JACS
JOURNAL OF THE AMERICAN CHEMICAL SOCIETY

Article

pubs.acs.org/JACS

Thermally Stable N_2-Intercalated WO_3 Photoanodes for Water Oxidation

Qixi Mi,[†] Yuan Ping,[‡] Yan Li,[§] Bingfei Cao,[⊥] Bruce S. Brunschwig,[†] Peter G. Khalifah,[*,⊥,∥] Giulia A. Galli,[*,‡] Harry B. Gray,[*,†] and Nathan S. Lewis[*,†]

[†]Beckman Institute and Kavli Nanoscience Institute, Division of Chemistry and Chemical Engineering, California Institute of Technology, M/C 127-72, 1200 East California Boulevard, Pasadena, California 91125, United States

[‡]Department of Chemistry, University of California, One Shields Avenue, Davis, California 95616, United States

[§]Computational Science Center and [⊥]Department of Chemistry Brookhaven National Laboratory, Upton, New York 11973, United States

[∥]Department of Chemistry, Stony Brook University, Stony Brook, New York 11974, United States

Supporting Information

ABSTRACT: We describe stable intercalation compounds of the composition $xN_2 \cdot WO_3$ ($x = 0.034-0.039$), formed by trapping N_2 in WO_3. The incorporation of N_2 significantly reduced the absorption threshold of WO_3; notably, $0.039N_2 \cdot WO_3$ anodes exhibited photocurrent under illumination at wavelengths ≤640 nm with a faradaic efficiency for O_2 evolution in 1.0 M $HClO_4$(aq) of nearly unity. Spectroscopic and computational results indicated that deformation of the WO_3 host lattice, as well as weak electronic interactions between trapped N_2 and the WO_3 matrix, contributed to the observed red shift in optical absorption. Noble-gas-intercalated WO_3 materials similar to $xN_2 \cdot WO_3$ are predicted to function as photoanodes that are responsive to visible light.

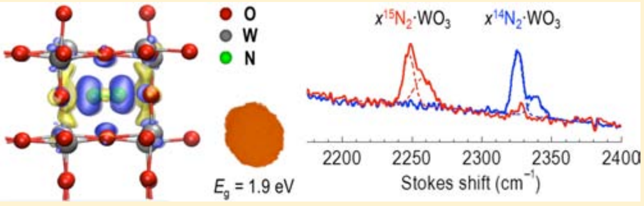

1. INTRODUCTION

Semiconducting metal oxide photocatalysts combine excellent stability under ambient conditions with high photoactivity, low cost, and nontoxicity.[1−6] Anodes made from n-type TiO_2, WO_3, and ZnO function in photoelectrochemical cells that convert sunlight into electricity and/or chemical fuels. These oxides are useful as photoelectrodes because at suitable pH values they exhibit stability to H_2O(l), O_2(g), and highly reactive hydroxyl radicals, as well as to other redox intermediates. The drawback is that the high band gap energies (E_g) of these materials [3.0 eV for rutile TiO_2,[7] 2.6 eV for WO_3,[8,9] and 3.3 eV for ZnO[10]] fall on the ultraviolet-and-blue tail of the solar spectrum.[11]

The conduction bands (CB) of these metal oxides consist of empty metal−oxygen antibonding orbitals, largely d−p π^* or s−p σ^* in character. In contrast, the valence bands (VB) are derived predominantly from nonbonding O 2p atomic orbitals, so the energies of the VB edges (E_{vb}) are not very sensitive to the metal ion or crystal polymorph.[5] A lower energy of the CB edge (E_{cb}) and/or a higher value of E_{vb}, both referenced to the vacuum level, will decrease E_g and thus enhance the absorption of visible light. A lower value of E_{cb} accompanies a symmetric arrangement of MO_6 octahedra, as higher symmetries enhance electron delocalization in the CB states.[12,13] For example, in the series of oxides having the formula $ATaO_3$ (A = Li, Na, K), the alkali metal ions A^+, whose electronic states do not directly contribute to the CB, play an important role by producing distortions of TaO_6 octahedra in the crystal structure. Hence, $KTaO_3$ exhibits the largest Ta−O−Ta bond angles (180°), the highest crystal symmetry ($Pm\bar{3}m$), and the lowest band gap (3.6 eV) in this group of metal oxides.[14] Introduction of a less electronegative element (such as N) into the crystal lattice leads to a higher value of E_{vb} [$Ta_2O_5 < TaON < Ta_3N_5$: E_{vb} values of −7.9, −6.6, and −6.0 V vs vacuum, respectively[15]].

Tungsten trioxide (WO_3) exhibits properties similar to those of the $ATaO_3$ compounds, most likely because the WO_3 crystal structure contains interconnected distorted WO_6 octahedra.[16] The CB edge of WO_3 is composed of W 5d−O 2p π^* orbitals, so E_{cb} of WO_3 is dependent on the W−O−W bond angle. The most stable phase of WO_3 at room temperature, monoclinic γ-WO_3, has a perovskite-like structure that is similar to that of $CaTiO_3$ and $NaTaO_3$, but does not contain an A-site ion (Figure 1A). The WO_6 octahedra optimize their packing through a distortion that results in tilted corner sharing of the octahedra ($\angle$W−O−W ≈ 158°). At elevated temperatures, monoclinic WO_3 adopts a more symmetric crystal structure, becoming orthorhombic between 330 and 740 °C, and then tetragonal (Figure 1B) between 740 °C and the melting point.[17] The evolution of the crystal structure of WO_3 is accompanied by a reduction in E_g from 2.6−2.7 eV at room temperature to ∼1.8 eV at 750 °C,[18] corresponding to a color change from pale yellow to red. This reversible variation in E_g,

Received: July 14, 2012
Published: September 28, 2012

© 2012 American Chemical Society

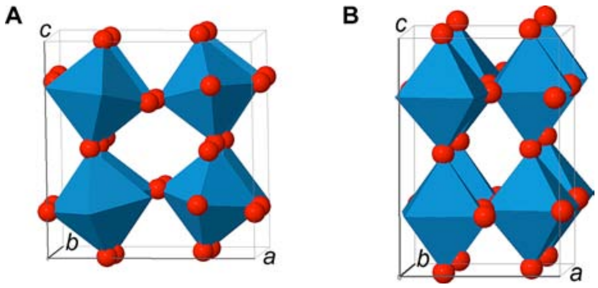

Figure 1. Unit cells of (A) monoclinic γ-WO_3 at room temperature[16] and (B) tetragonal WO_3 at 800 °C.[17] W atoms are located inside the blue octahedra, and O atoms are represented by red spheres. The void spaces can accommodate small cations and molecules.

induced structurally, does not involve a change in stoichiometry. Moreover, a cubic phase of WO_3 prepared at 0.66 GPa, 700 °C and then returned to ambient conditions has been reported to be "ruby red" in color.[19] The strong correlation between the crystal structure and band gap of WO_3 is of wide interest, and theory[20−22] has suggested that the E_g values of different WO_3 phases decrease in the order monoclinic > orthorhombic > tetragonal ≥ cubic, although the computed band gaps systematically underestimate the experimental values.

We report herein that the absorption threshold of WO_3 can be lowered by incorporation of N_2 into the WO_3 crystal structure, forming compounds represented by the formula $xN_2{\cdot}WO_3$. Spectroscopic and theoretical methods were performed on these intercalation compounds to study the emergent properties of the trapped N_2 and the WO_3 matrix as a result of the host−guest interaction. Photoelectrochemical experiments on electrodes made from $xN_2{\cdot}WO_3$ showed that this photoanode material was responsive to visible light of $\lambda \leq$ 640 nm, which is consistent with the optical band gap (1.9 eV) of $xN_2{\cdot}WO_3$. Based on these results, we propose a mechanism to account for the reduced band gap of $xN_2{\cdot}WO_3$, and predict that WO_3 intercalated with a noble gas will likewise exhibit a band gap narrower than that of pure WO_3.

2. EXPERIMENTAL SECTION

Chemicals. Tungsten powder (Aldrich 510106), tungstic acid (H_2WO_4, Alfa Aesar 82118), ammonium metatungstate (AMT, $(NH_4)_6H_2W_{12}O_{40}{\cdot}xH_2O$, Alfa Aesar 44792), ammonium paratungstate (APT, $(NH_4)_{10}H_2W_{12}O_{42}{\cdot}4H_2O$, Aldrich 510114), ammonium-^{15}N hydroxide ($^{15}NH_4OH$, Cambridge Isotope Laboratories NLM-1320, 3.3 N, 98+% ^{15}N), 1.0 M NaOH (EMD Chemicals SX0607H), and 1.0 M HCl (J. T. Baker 5620) were obtained commercially.

Ammonium-^{15}N paratungstate tetrahydrate (APT-^{15}N) was synthesized by dissolution of H_2WO_4 in aqueous $^{15}NH_4OH$ followed by evaporative crystallization. The intercalation compounds $xN_2{\cdot}WO_3$ (x = 0.034−0.039) were prepared by thermolysis with a stepwise temperature ramp of APT or AMT in a stream of $O_2(g)$. For preparing $0.039^{15}N_2{\cdot}WO_3$, a weighed 20-ml vial that contained 0.5002 g (159.2 μmol) of crystalline $(^{15}NH_4)_{10}$ $[H_2W_{12}O_{42}]{\cdot}4H_2O$ was placed horizontally, close to a thermocouple, in a tube furnace. A gentle stream of O_2 (10 sccm·s^{-1}) was delivered into the vial using a Pasteur pipette. The temperature was brought to 350 and 390 °C successively each for 30 min, and finally to 420 °C for 1 h. The solids appeared yellow, orange-red, and brown, at the respective temperatures. After cooling to room temperature, the product turned orange-red and weighed 0.4453 g (1.911 mmol, quantitative yield).

Sample Characterizations. Raman spectra were measured at room temperature on a Renishaw Raman microscope using 514.5-nm excitation and a Si wavenumber standard. ^{15}N solid-state NMR spectra were measured on a Bruker Avance 500 MHz NMR spectrometer under magic-angle spinning at 10 kHz. EPR experiments were performed on a Bruker EMX X-band EPR spectrometer at 77 K. Magnetic susceptibility data were obtained on a Quantum Design magnetic properties measurement system at 20−300 K. Diffuse reflectance spectra were measured on a Shimadzu UV-2101 spectrophotometer equipped with an integrating sphere using a $BaSO_4$ white reference. Elemental analysis was carried out by Columbia Analytical Services (Tucson, AZ).

The amount of N_2 trapped in WO_3 was measured by the volume of evolved gas after $xN_2{\cdot}WO_3$ had been decomposed. The plunger of a 3-mL plastic syringe was detached and a piece of cotton was placed in the nozzle. An accurately weighed sample (0.1−0.2 g) of $xN_2{\cdot}WO_3$ and a small magnetic stir bar were loaded in the syringe body. Then the plunger was replaced, and the syringe body was filled with 3.0 mL of 1.0 M NaOH by suction. After air bubbles had been expelled, the syringe was held above a stir plate, and the solution that was displaced by evolution of N_2 was collected in a vial below the syringe. Once $xN_2{\cdot}WO_3$ had completely dissolved, the volume of the displaced solution was measured using a calibrated micropipette. The entire experiment was performed under 20 °C, 1 atm, and in stagnant air.

Powder X-ray diffraction (XRD) data were collected on a Bruker D8 Advance powder diffractometer (300 mm radius, θ−θ geometry) with a Cu Kα source, a 192-channel LynxEye detector, and a fixed divergent slit width of 0.6°. Samples were filled into a zero-background Si holder with a well depth of 0.3 mm. The TOPAS v4.2 software package was used for data fitting. Substantial broadening of the XRD peaks of $xN_2{\cdot}WO_3$ was observed, and use of whole pattern fitting to model the θ-dependence of peak widths showed that this broadening was primarily due to strain rather than particle size effects.

Photoelectrochemistry. Samples of SnO_2:F-coated glass slides (FTO, Hartford Glass, TEC 15) were cut into pieces 1.0 cm in width and cleaned with water and ethanol. The slides were placed on a hot plate at 300−320 °C with the conductive side facing up, and 10−20-mL precursor solutions were manually sprayed using an airbrush (Iwata Revolution BCR) in 1-s pulses. To prepare $0.039N_2{\cdot}WO_3$ photoanodes, a 1.0% (w/v) aqueous solution of ammonium metatungstate was used in the spray. Subsequently, the glass slides were transferred into a furnace and heated up slowly to 420 °C in a stream of $O_2(g)$, using the same methods as those to produce the $0.039^{15}N_2{\cdot}WO_3$ powders. For pure WO_3 photoanodes, an aqueous solution of peroxytungstic acid[23] (50 mM in W) was used and the glass slides were annealed at 450 °C for 1 h in a preheated furnace. Profilometry (Dektak 3030) indicated that these films were ~3 μm thick.

The photoelectrochemical cell consisted of a photoanode ($0.039N_2{\cdot}WO_3$ or pure WO_3 on conductive glass) as the working electrode, a Pt mesh counter electrode, a reference electrode (Ag/AgCl/3.0 M NaCl, Bioanalytical Systems, Inc.), and 1.0 M HCl(aq) as the electrolyte. These components were positioned in a 25-mL, three-neck, round-bottom flask that had been fitted with a fused silica window (25 mm in diameter) using an epoxy adhesive (Loctite Hysol 9460). The photoanode was illuminated from the interface between the metal oxide film and the conductive glass substrate. A Gamry Series G 300 potentiostat was used to record the photocurrents generated by the working electrode at the formal potential of the Cl^-/Cl_2 couple (E = 1.20 V vs Ag/AgCl).

Spectral response measurements were performed using ultraviolet and visible light that was emitted from a 150-W Xe arc lamp, chopped at 3.0 Hz, and passed through a monochromator with 0.5-mm-wide slits. A photoelectrochemical cell or a calibrated Si photodiode (OSI Optoelectronics, UV-50) was positioned in the light path, so that the illuminated surface spot was focused to less than 1×3 mm^2 in size. At each wavelength, photocurrents were measured with lock-in detection, and the external quantum yield (Φ_{ext}) of the photoelectrochemical cell was calculated based on the known Φ_{ext} values of the calibrated Si diode. To compensate for fluctuations in the intensity of the monochromatic illumination, a small fraction of the light beam was split using a quartz plate and was continuously monitored by another Si photodiode. The internal quantum yield (Φ) was calculated by dividing Φ_{ext} by the light absorption of the photoanode, which was measured by use of a Cary 5000 UV−vis spectrophotometer in which the photoanode has been placed in the center of an integrating sphere. A piece of SnO_2:F-coated glass served as the blank in the absorption measurements.

Photoelectrochemical water oxidation was performed in 1.0 M $HClO_4$(aq) under two-electrode and galvanostatic conditions, and the production of dissolved O_2 was monitored in real time by a fluorescent O_2 sensor.[24]

3. RESULTS AND DISCUSSION

APT decomposes into amorphous AMT between 230 and 325 °C, losing H_2O(g) and NH_3(g) at higher temperatures, and eventually crystallizes exothermically at ∼410 °C as orthorhombic WO_3.[25−29] However, if the O_2(g) flow is sufficiently strong, part of the NH_4^+ in the solid state can be oxidized to N_2(g), in a process presumably catalyzed by tungsten. If the temperature is increased slowly during the phase transition at ∼410 °C, some of the N_2 enclosed in the solid state is trapped in the hollow center of the newly crystallized WO_3 lattice, leading to a stable intercalation compound. When heated in an oxygen atmosphere several metal oxynitride perovskites of lanthanum/titanium and strontium/niobium have been shown to trap N_2 in the crystal lattice, as evidenced by thermogravimetric analysis, X-ray photoelectron spectroscopy and Raman spectroscopy.[30−34]

To identify the chemical origin of the trapped N_2, ^{15}N-labeled APT, which was prepared from tungstic acid and $^{15}NH_3 \cdot H_2O$, was converted to $x^{15}N_2 \cdot WO_3$, which exhibited strong Raman (Figure 2) and solid-state NMR (Figure S1) signals characteristic of $^{15}N_2$, even after annealing in air at temperatures up to 750 °C. The chemical compositions of the unlabeled intercalation compounds that had been annealed at 420, 550, and 600 °C were determined by gravimetric, gasometric, and elemental analyses to be 99.54% by weight WO_3, 0.47% N_2 and ≤0.02% N(−3), with an error range of ±0.02%. These results established the empirical formula to be $xN_2 \cdot WO_3$, with $x = 0.039$, for annealing temperatures from 420 to 600 °C. Samples that had been annealed at 750 °C gave $x = 0.034$. Decomposition of AMT under stagnant air in an oven that had been preheated to 450 °C produced the metastable phase of hexagonal WO_3[35,36] with only 0.01% by weight of trapped N_2. Electron paramagnetic resonance and magnetic susceptibility measurements confirmed that all of these intercalation compounds were diamagnetic, and thus did not contain detectable NO(g) or NO_2(g).

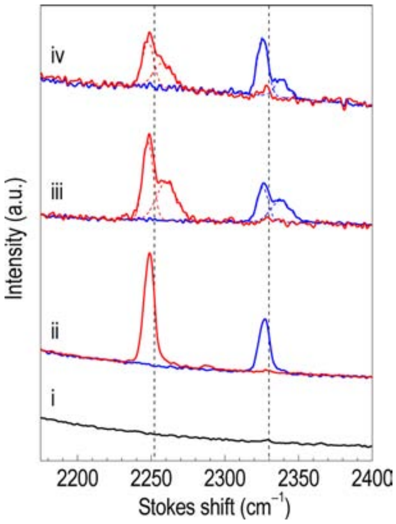

Figure 2. Room-temperature Raman spectra of (i) pure monoclinic WO_3, (ii) $0.034N_2 \cdot WO_3$ annealed at 750 °C, (iii) $0.039N_2 \cdot WO_3$ annealed at 550 °C, and (iv) $0.039N_2 \cdot WO_3$ annealed at 420 °C. The solid red and blue curves indicate samples with and without ^{15}N labeling, respectively. The two dashed vertical lines denote the Stokes shifts of (left) $^{15}N_2$(g) and (right) $^{14}N_2$. The dashed red and blue curves show the deconvolution of the observed signal into two Gaussian peaks. a.u. = arbitrary units.

Figure 2 depicts the N≡N vibrational frequencies measured by microscopic Raman spectroscopy at room temperature for $x^{14}N_2 \cdot WO_3$ and $x^{15}N_2 \cdot WO_3$. The Raman spectra showed an isotopic shift (1.035) equal to that observed for $^{14}N_2$(g)[37] relative to $^{15}N_2$(g).[38] The unlabeled intercalation compounds showed an intense peak at 2326 cm^{-1} and, in the case of $0.039N_2 \cdot WO_3$, another broad peak was observed at 2338 cm^{-1}, which implies that at least two configurations of N_2 were present in $0.039N_2 \cdot WO_3$. These spectroscopic features are consistent with N_2 experiencing a weak electronic interaction with the WO_3 lattice, but are in contrast to the Raman frequency of $^{14}N_2$ in the gas phase (2330 cm^{-1}) or in previously known clathrates (2321−2327 cm^{-1}, Table S1). The Raman spectra of the LaTiON perovskites exhibit a broad N_2 peak at ∼2328 cm^{-1}, whereas the spectra of the (La,Ca)TiON compounds show two broad peaks, similar to the spectra observed herein, at ∼2344 and ∼2352 cm^{-1}.[31−34]

The structural properties of WO_3 and $xN_2 \cdot WO_3$ were investigated using density functional theory (DFT) within the local density approximation (LDA). The computed equilibrium crystal structure of monoclinic WO_3 at room temperature was in excellent agreement with experiment, with a 0.9% underestimate of the unit cell volume (Table S2). When N_2 was inserted into the hollow center of WO_3 along different crystallographic directions, at a concentration of 1 N_2 per 8 WO_3 units, the calculated difference between the relaxed lattice constants *a* and *b* (Figure 1A) of the resulting intercalation compound was reduced from 0.10 Å to 0.004 Å, and the cell volume expanded by ∼5%. The energy change for incorporation of N_2 into WO_3, and the kinetic barrier (Figure S2) for N_2 to diffuse from a hollow center of the WO_3 crystal to a neighboring hollow center, were computed to be 1.7−1.9 and 2.6 eV, respectively, indicating that $xN_2 \cdot WO_3$ should be kinetically stable (thermal energy $RT = 0.067$ eV at 750 °C).

A series of computational models was constructed to gain insight into the geometry of the trapped N_2 molecules. DFT calculations indicated that the WO_3 matrix exerted a net repulsive effect upon the N_2 guest molecule, due to the endoergic nature of the inclusion of N_2 (Figure 3). Specifically,

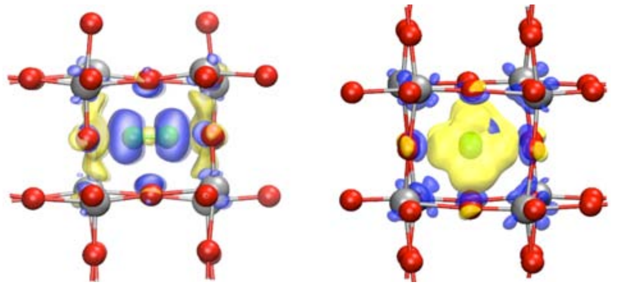

Figure 3. Isosurface of electron density difference for monoclinic WO_3 with and without N_2, viewed from two perspectives: yellow, electron loss; blue, electron gain. Atoms: silver, W; red, O; green, N.

for N_2 oriented along the [100], [010], or [001] crystallographic direction, the N≡N bond length was reduced by 0.003 Å and the stretching frequency increased by 6–8 cm^{-1} relative to corresponding values for $N_2(g)$. The total energies of these three geometrical arrangements of trapped N_2 were calculated to differ from one another by <0.1 eV, suggesting that all of these configurations may be populated within an individual macroscopic sample. The coexistence of multiple configurations of trapped N_2 is presumably responsible for the broad, blue-shifted shoulders apparent in the spectra shown in Figure 2. On the other hand, the N–W distance became the shortest when the trapped N_2 was aligned along the [111] crystallographic direction. As a result, partial charge transfer occurred from N_2 bonding orbitals to the WO_3 matrix. The N≡N bond was weakened (calculated ~10 cm^{-1} red shift in the stretching frequency), in accord with experiment (red-shifted Raman peaks, see Figure 2).

The weak interaction between trapped N_2 and the WO_3 matrix also had a noticeable influence on the host lattice. The XRD pattern of $xN_2 \cdot WO_3$ measured at room temperature (Figure 4) was similar to that of a lightly doped tungsten bronze $Na_{0.025}WO_3$,[39] and refinement of the patterns revealed systematic deformations in the crystal lattices of these compounds (Figure S3, Table S3). Temperature-dependent XRD experiments[17] have revealed that pure WO_3 transforms from a monoclinic phase (Figure 1A, lattice parameters a = 7.31 Å, b = 7.54 Å, c = 7.69 Å, β = 90.9°) at room temperature to a tetragonal phase (Figure 1B, a = b = 7.46 Å, c = 7.85 Å) at 800 °C, with the a and b parameters converging as the temperature increases. The a:b ratio of the $xN_2 \cdot WO_3$ samples increased from 0.974 to 0.980 with decreasing annealing temperatures. These values all exceeded that of pure monoclinic WO_3 (0.970), signifying that the intercalation of N_2 into the WO_3 lattice occurred at all temperatures, to the greatest degree at the lowest treatment temperature (Figure 4). These observations suggest that the introducation of N_2 into WO_3 likely hindered the tilting modes of the WO_6 octahedra and resulted in the formation of domains with a local symmetry higher than monoclinic. In terms of the Raman spectra of the WO_3 matrix (Figure S4), the broad features displayed in $xN_2 \cdot WO_3$ but not in pure monoclinic WO_3 do not allow definitive identification of the symmetry of the crystal phase(s) of $xN_2 \cdot WO_3$, because the Raman frequencies of the O–W–O vibrational modes do not vary significantly among various phases of WO_3.[40]

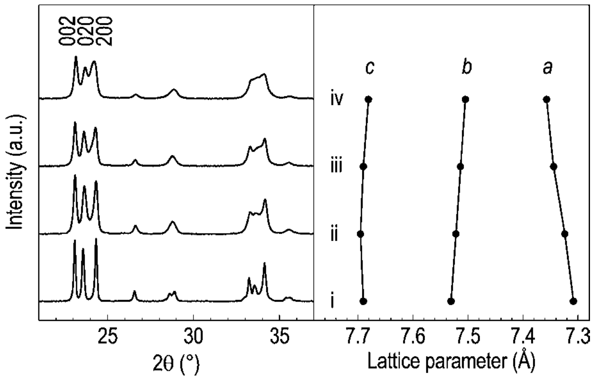

Figure 4. (Left) X-ray diffraction patterns and (right) lattice parameters of samples (i) pure monoclinic WO_3; (ii) $0.034N_2 \cdot WO_3$ annealed at 750 °C; (iii) $0.039N_2 \cdot WO_3$ annealed at 550 °C; and (iv) $0.039N_2 \cdot WO_3$ annealed at 420 °C. The 002, 020, and 200 peak positions reflect the a, b, and c lattice parameters, respectively. Statistical errors in the lattice parameters are smaller than the size of the solid circles.

The subtle structural modifications caused by N_2 insertion in the WO_3 matrix gave rise to striking changes in color, from the pale yellow of pure monoclinic WO_3 to the orange red of $0.039N_2 \cdot WO_3$ that had been annealed at 420 °C. Figure 5A plots the room-temperature diffuse reflectance spectra of $xN_2 \cdot WO_3$ as $(Fh\nu)^{1/2}$ vs $h\nu$, where $F = (1 - R)^2/2R$ is the Kubelka–Munk absorption coefficient (R is the reflectance) and $h\nu$ is the photon energy. The onset of light absorption was extrapolated to determine the indirect E_g of $xN_2 \cdot WO_3$.[41] In contrast to pure monoclinic WO_3, which has been previously[8,9] shown to exhibit an indirect E_g of 2.6 eV, $0.039N_2 \cdot WO_3$ exhibited a significantly reduced E_g of 1.9–2.0 eV, with the exact value dependent on the annealing temperature. For $0.034N_2 \cdot WO_3$ that had been annealed at 750 °C, this low-energy absorption feature was not detected; instead, an

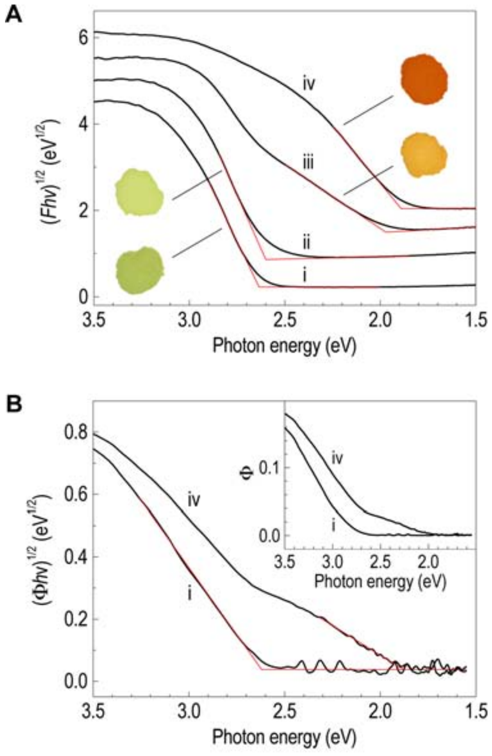

C

Sample	Optical E_g (eV)	Photoelectrochemical E_g (eV)
i	2.6	2.6
ii	2.6	Not measured
iii	2.0	Not measured
iv	1.9	1.9

Figure 5. (A) Diffuse reflectance spectra (vertically offset for clarity) and photographs, (B) spectral response data, and (C) indirect band gaps of (i) pure monoclinic WO_3; (ii) $0.034N_2 \cdot WO_3$ annealed at 750 °C; (iii) $0.039N_2 \cdot WO_3$ annealed at 550 °C; and (iv) $0.039N_2 \cdot WO_3$ annealed at 420 °C. The spectral response data, plotted as $(\Phi h\nu)^{1/2}$ and Φ vs $h\nu$, were measured during the potentiostatic photoanodic oxidation of 1.0 M HCl(aq) to $Cl_2(g)$. In both (A) and (B) the optical band gaps of these materials were determined by extrapolation of the onset of $(Fh\nu)^{1/2}$ or $(\Phi h\nu)^{1/2}$ vs $h\nu$.

absorption band at $h\nu \geq 2.6$ eV, similar to that of pure monoclinic WO_3, was observed.

An oxygen deficiency in the metal oxide is unlikely to cause the red shift in optical absorption, because the intercalation compounds were prepared under 1 atm $O_2(g)$, and because diffuse reflectance spectra of these samples (Figure 5A) did not show significant absorption in the red and near-infrared regions. Oxygen-deficient WO_{3-x} absorbs light strongly in these regions, and is deep blue.[27] Atomic N doping also is unlikely to cause the absorption shift, because the diamagnetism, and oxidation stability of $x N_2 \cdot WO_3$, do not match the predicted properties of N-doped WO_3, whose existence remains elusive to date. Previous studies of N-doped TiO_2[42−45] have shown that the N dopants exist as isolated paramagnetic centers, and that the N dopants can be oxidized by the TiO_2 lattice to produce NO_x and/or N_2. Furthermore, N-doped perovskites do not yield a Raman signal at ~2330 cm^{-1}, whereas perovskites that have trapped N_2 species show this charastetic vibrational signal.[31−34] The tendency for N dopants to be oxidized by the WO_3 lattice is expected to be even more pronounced, because the potential of the conduction-band edge of WO_3 (0.4 V vs NHE) is more positive than that of TiO_2 (−0.2−0.0 V vs NHE). The diffuse reflectance spectrum of $0.039N_2 \cdot WO_3$ exhibited an absorption band at $h\nu \geq 2.6$ eV and an additional absorption feature at $h\nu \geq 1.9-2.0$ eV. Tetragonal WO_3 exhibits an E_g that has been experimentally determined[18] to be ~1.8 eV at 750 °C and has been theoretically shown[21] to be an indirect band gap, so similar structural characteristics may be present in $0.039N_2 \cdot WO_3$ at room temperature (tetragonal WO_3 is stable only above 740 °C). Because of the nonequilibrium synthetic procedure, it is possible that the WO_3 matrix of $0.039N_2 \cdot WO_3$ is heterogeneous. Both the Raman and diffuse reflectance spectra are consistent with the coexistence of two crystal phases within $0.039N_2 \cdot WO_3$ annealed at 420 or 550 °C. Similarly, the XRD patterns of these samples could not be accurately reproduced without modeling either a two-phase mixture or an asymmetric strain gradient.

The band-gap narrowing of $x N_2 \cdot WO_3$ was evaluated by DFT calculations. Insertion of N_2 into a *fixed* monoclinic WO_3 lattice did not markedly perturb the E_{cb} value, and the CB remained dominated by the W 5d−O 2p π^* orbitals. Instead, the N 2p orbitals contributed partially to the VB (Figure S6) and shifted E_{vb} to higher values. As a result, the E_g value decreased by ~0.1 eV at low N_2-to-WO_3 ratios (1:8 or 2:8), and by as much as 0.7 eV at a 1:1 ratio. When the WO_3 lattice was *relaxed* with trapped N_2 at a 1:8 (N_2:WO_3) ratio, the calculations indicated that the tilt angles (∠W−O−W) between adjacent WO_6 octahedra increased from 155−165° to 170−175°, while the W−O bond lengths were only weakly affected (on average by 0.017 Å). The unfolded W−O−W tilt angle, along with converging values of the calculated lattice constants *a* and *b*, suggested that $N_2 \cdot 8WO_3$ adopted a crystal structure that was analogous to that of tetragonal WO_3. DFT calculations at different levels (LDA and hybrid functionals, Table S4) indicated that the E_g value of such a tetragonal-like WO_3 structure, regardless of the presence of trapped N_2, was reduced by 0.2 eV from that of monoclinic WO_3. These results, which are in qualitative agreement with the experimental data, thus provide a self-consistent physical interpretation of the observed red shift in optical absorption upon insertion of N_2 into WO_3.

The utility of $0.039N_2 \cdot WO_3$ as a photoanode material was evaluated by photoelectrochemistry. Thin films, one of $0.039N_2 \cdot WO_3$ and the other of pure monoclinic WO_3 (~3 μm in thickness), were deposited on conducting glass substrates by spray thermolysis from aqueous solutions of either AMT (for $0.039N_2 \cdot WO_3$) or peroxytungstic acid (for pure WO_3).[23] The internal quantum yield (Φ) of these photoanodes as a function of wavelength (λ) was measured during photoelectrochemical oxidation of 1.0 M HCl(aq) to $Cl_2(g)$ under monochromatic illumination at a controlled electrode potential of 1.20 V vs a Ag/AgCl reference electrode. From an interfacial electron-transfer perspective, the Cl^-/Cl_2 couple served as a kinetically more rapid surrogate for the H_2O/O_2 couple.[46] Figure 5B shows that pure monoclinic WO_3 required $h\nu \geq 2.6$ eV photons ($\lambda \leq 470$ nm) to generate a photocurrent, whereas $0.039N_2 \cdot WO_3$ that had been annealed at 420 °C was responsive to $h\nu \geq 1.9$ eV photons ($\lambda \leq 640$ nm), both determined by extrapolation of $(\Phi h\nu)^{1/2}$ vs $h\nu$.[35] These values agreed with the indirect E_g of the photoanode materials as measured by diffuse reflectance spectroscopy (Figure 5C). The O_2 evolution at $0.039N_2 \cdot WO_3$ photoanodes was examined by two-electrode, galvanostatic (photo)electrolysis of 1.0 M $HClO_4$(aq).[24] Figure 6 shows typical results for a $0.039N_2 \cdot WO_3$ photoanode at a constant photocurrent of 0.50 mA (and a photocurrent density of ~0.3 $mA \cdot cm^{-2}$) for 2000 s. The amount of O_2 produced using a $0.039N_2 \cdot WO_3$ electrode in two runs was 80 ± 3 μg, which corresponded to a faradaic efficiency of nearly unity. Under the same conditions, a RuO_2 electrode operated in the dark under galvanostatic control produced 80 μg of O_2, with a theoretical yield of 83 μg. The $0.039N_2 \cdot WO_3$ photoanode generated a photovoltage under illumination, and thus required lower cell voltages (~1.4 V) than the dark RuO_2 electrode (~1.7 V) to maintain the constant electrolytic currents (Figure S7). Essentially no change was observed in the Raman signals of the trapped N_2 before and after the photoelectrolysis (Figure S8).

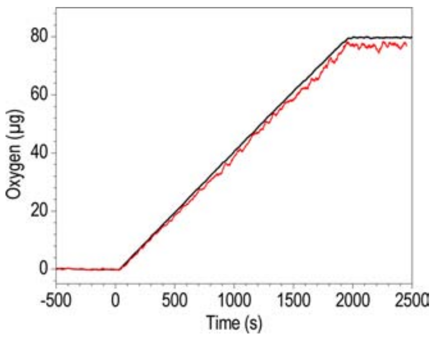

Figure 6. Production of dissolved O_2 during (photo)electrolysis of 1.0 M $HClO_4$ at constant current (0.50 mA, 2000 s). Red: Typical results from a $0.039N_2 \cdot WO_3$ photoanode under simulated sunlight. Black: Results from a RuO_2 electrode in the dark.

These results imply that the dominant interaction between the N_2 and the WO_3 lattice is steric in origin, forcing the WO_6 octahedra into a more symmetric arrangement within the crystal lattice. This lack of significant electronic interaction would suggest that similar shifts in the band gap can be achieved by the incorporation of other inert molecules or atoms into the framework. Ab initio calculations predict that the insertion of noble gas atoms (Ne, Ar, Kr, and Xe) into WO_3 will modify the crystal structure and reduce E_g relative to that of pure WO_3.[47] The calculated reduction in E_g is substantial (0.9 eV) for Xe, whose 6p atomic orbital raised the E_{vb} by 0.8 V.[47]

4. CONCLUSIONS

The intercalation compounds of formula $0.039N_2{\cdot}WO_3$ thus exhibited enhanced absorption of sunlight compared with pure WO_3, as well as extraordinary thermal stability. A weak electronic interaction between trapped N_2 molecules and the WO_3 matrix resulted in a faster-vibrating configuration of the former and a local deformation of the latter. These electronic and structural effects brought the CB and VB edges closer in energy, which in turn significantly lowered the E_g of $0.039N_2{\cdot}WO_3$ relative to that of pure monoclinic WO_3. A diverse family of intercalated WO_3, $xA{\cdot}WO_3$, has yet to be explored, where A is a small neutral molecule (e.g., N_2, CO, and CO_2) or a noble gas atom. According to ab initio calculations, the insertion of noble gas atoms (Ne, Ar, Kr and Xe) into WO_3 is expected to reduce E_g relative to WO_3. Through the use of more forcing conditions during preparation, it should be possible to incorporate higher concentrations of N_2 or noble gases into WO_3, which likely will result in a homogeneous WO_3 matrix with higher lattice symmetry, as well as more intense light absorption in the 470−640 nm range than was observed for $0.039N_2{\cdot}WO_3$.

■ ASSOCIATED CONTENT

Supporting Information

Details of inorganic synthesis, XRD refinement, and theoretical calculations, as well as ^{15}N solid-state NMR and Raman spectra of the samples. This material is available free of charge via the Internet at http://pubs.acs.org.

■ AUTHOR INFORMATION

Corresponding Author

kpete@bnl.gov; gagalli@ucdavis.edu; hbgray@caltech.edu; nslewis@caltech.edu

Notes

The authors declare no competing financial interest.

■ ACKNOWLEDGMENTS

We thank Prof. George R. Rossman for discussions and for assistance with the Raman microscope, and Prof. Francois Gygi for discussions of ab initio calculations. This work was supported by the National Science Foundation (NSF) Powering the Planet Center for Chemical Innovation (CCI-Solar), Grants CHE-0802907 and CHE-0947829. Q.M. was a CCI-Solar Postdoctoral Fellow. P.G.K. thanks the support of the U.S. Department of Energy under the Hydrogen Fuel Initiative. Research was in part carried out in the Molecular Materials Research Center of the Beckman Institute of the California Institute of Technology, and in part carried out at Brookhaven National Laboratory under No. DE-AC02-98CH10886 with the U.S. Department of Energy. Use of the Teragrid computational facilities is gratefully acknowledged.

■ REFERENCES

(1) Boddy, P. J. *J. Electrochem. Soc.* **1968**, *115*, 199−203.
(2) Fujishima, A.; Honda, K. *Nature* **1972**, *238*, 37−38.
(3) Kung, H. H.; Jarrett, H. S.; Sleight, A. W.; Ferretti, A. *J. Appl. Phys.* **1977**, *48*, 2463−2469.
(4) Hardee, K. L.; Bard, A. J. *J. Electrochem. Soc.* **1977**, *124*, 215−224.
(5) Nozik, A. J. *Annu. Rev. Phys. Chem.* **1978**, *29*, 189−222.
(6) Kudo, A.; Miseki, Y. *Chem. Soc. Rev.* **2009**, *38*, 253−278.
(7) Cronemeyer, D. C. *Phys. Rev.* **1952**, *87*, 876−886.
(8) Butler, M. A. *J. Appl. Phys.* **1977**, *48*, 1914−1920.
(9) Koffyberg, F. P.; Dwight, K.; Wold, A. *Solid State Commun.* **1979**, *30*, 433−437.
(10) Srikant, V.; Clarke, D. R. *J. Appl. Phys.* **1998**, *83*, 5447−5451.
(11) Bolton, J. R.; Strickler, S. J.; Connolly, J. S. *Nature* **1985**, *316*, 495−500.
(12) Wiegel, M.; Emond, M. H. J.; Stobbe, E. R.; Blasse, G. *J. Phys. Chem. Solids* **1994**, *55*, 773−778.
(13) Woodward, P. M.; Mizoguchi, H.; Kim, Y. I.; Stoltzfus, M. W. The Electronic Structure of Metal Oxides. In *Metal oxides: Chemistry and applications*; Fierro, J. L. G., Ed.; Taylor & Francis: Boca Raton, FL, 2006; pp 133−193.
(14) Kato, H.; Kudo, A. *J. Phys. Chem. B* **2001**, *105*, 4285−4292.
(15) Chun, W. J.; Ishikawa, A.; Fujisawa, H.; Takata, T.; Kondo, J. N.; Hara, M.; Kawai, M.; Matsumoto, Y.; Domen, K. *J. Phys. Chem. B* **2003**, *107*, 1798−1803.
(16) Loopstra, B. O.; Rietveld, H. M. *Acta Crystallogr. B* **1969**, *25*, 1420−1421.
(17) Vogt, T.; Woodward, P. M.; Hunter, B. A. *J. Solid State Chem.* **1999**, *144*, 209−215.
(18) Iwai, T. *J. Phys. Soc. Jpn.* **1960**, *15*, 1596−1600.
(19) Crichton, W. A.; Bouvier, P.; Grzechnik, A. *Mater. Res. Bull.* **2003**, *38*, 289−296.
(20) Cora, F.; Patel, A.; Harrison, N. M.; Dovesi, R.; Catlow, C. R. A. *J. Am. Chem. Soc.* **1996**, *118*, 12174−12182.
(21) Chatten, R.; Chadwick, A. V.; Rougier, A.; Lindan, P. J. D. *J. Phys. Chem. B* **2005**, *109*, 3146−3156.
(22) Gonzalez-Borrero, P. P.; Sato, F.; Medina, A. N.; Baesso, M. L.; Bento, A. C.; Baldissera, G.; Persson, C.; Niklasson, G. A.; Granqvist, C. G.; da Silva, A. F. *Appl. Phys. Lett.* **2010**, *96*, 061909.
(23) Meulenkamp, E. A. *J. Electrochem. Soc.* **1997**, *144*, 1664−1671.
(24) Mi, Q. X.; Zhanaidarova, A.; Brunschwig, B. S.; Gray, H. B.; Lewis, N. S. *Energ. Environ. Sci.* **2012**, *5*, 5694−5700.
(25) Neugebauer, J.; Hegedüs, A. J.; Millner, T. Z. *Anorg. Allg. Chem.* **1959**, *302*, 50−59.
(26) Kohlstrung, G. *Phys. Status Solidi* **1962**, *2*, 85−96.
(27) Lassner, E.; Schubert, W.-D. *Tungsten: Properties, chemistry, technology of the element, alloys, and chemical compounds*; Kluwer Academic/Plenum Publishers: New York, 1999.
(28) Madarasz, J.; Szilagyi, I. M.; Hange, F.; Pokol, G. *J. Anal. Appl. Pyrolysis* **2004**, *72*, 197−201.
(29) Fait, M.; Lunk, H. J.; Feist, M.; Schneider, A.; Dann, J. N.; Frisk, T. A. *Thermochim. Acta* **2008**, *469*, 12−22.
(30) Le Gendre, L.; Marchand, R.; Laurent, Y. *J. Eur. Ceram. Soc.* **1997**, *17*, 1813−1818.
(31) Le Gendre, L.; Marchand, R.; Piriou, B. *Eur. J. Solid State Inorg. Chem.* **1997**, *34*, 973−982.
(32) Tessier, F.; Le Gendre, L.; Chevire, F.; Marchand, R.; Navrotsky, A. *Chem. Mater.* **2005**, *17*, 3570−3574.
(33) Ebbinghaus, S. G.; Abicht, H.-P.; Dronskowski, R.; Mueller, T.; Reller, A.; Weidenkaff, A. *Prog. Solid State Chem.* **2009**, *37*, 173−205.
(34) Rachel, A.; Ebbinghaus, S. G.; Gungerich, M.; Klar, P. J.; Hanss, J.; Weidenkaff, A.; Reller, A. *Thermochim. Acta* **2005**, *438*, 134−143.
(35) Cheng, K. H.; Jacobson, A. J.; Whittingham, M. S. *Solid State Ionics* **1981**, *5*, 355−358.
(36) Szilagyi, I. M.; Wang, L. S.; Gouma, P. I.; Balaszsi, C.; Madarasz, J.; Pokol, G. *Mater. Res. Bull.* **2009**, *44*, 505−508.
(37) Bendtsen, J.; Rasmussen, F. *J. Raman Spectrosc.* **2000**, *31*, 433−438.
(38) Bendtsen, J. *J. Raman Spectrosc.* **2001**, *32*, 989−995.
(39) Paul, S.; Mukherjee, G. D.; Ghosh, A.; Oishi, S.; Raj, S. *Appl. Phys. Lett.* **2011**, *98*, 121910.
(40) Pecquenard, B.; Lecacheux, H.; Livage, J.; Julien, C. *J. Solid State Chem.* **1998**, *135*, 159−168.
(41) The alternative plots for a direct band gap, $(Fh\nu)^2$ vs $h\nu$, do not display a well-defined region for extrapolation; see Figure S5.
(42) Mwabora, J. M.; Lindgren, T.; Avendano, E.; Jaramillo, T. F.; Lu, J.; Lindquist, S. E.; Granqvist, C. G. *J. Phys. Chem. B* **2004**, *108*, 20193−20198.

(43) Di Valentin, C.; Pacchioni, G.; Selloni, A.; Livraghi, S.; Giamello, E. *J. Phys. Chem. B* **2005**, *109*, 11414−11419.

(44) Nambu, A.; Graciani, J.; Rodriguez, J. A.; Wu, Q.; Fujita, E.; Sanz, J. F. *J. Chem. Phys.* **2006**, *125*, 094706.

(45) Reyes-Garcia, E. A.; Sun, Y. P.; Reyes-Gil, K.; Raftery, D. *J. Phys. Chem. C* **2007**, *111*, 2738−2748.

(46) Hill, J. C.; Choi, K. S. *J. Phys. Chem. C* **2012**, *116*, 7612−7620.

(47) Ping, Y.; Li, Y.; Gygi, F.; Galli, G. A. *Chem. Mater.* **2012**, submitted.